Supplemental Materials Inventory:

I. Supplementary Figures

Figure S1 (related to Figure 1): Influence of different parameters on the length-dependent model in 3D

Figure S2 (related to Figure 2): Tests of hypotheses and parameters for zebrafish cleavage patterns.

Figure S3 (related to Figure 2): Influence of shape parameters on the prediction of zebrafish cleavage and embryo morphogenesis.

Figure S4 (related to Figure 3): Influence of yolk and shape parameters on the prediction of Xenopus cleavage and embryo morphogenesis.

Figure S5 (related to Figure 4, 5 and 6): Evidence and characteristics of MT branching in interphase asters in sea urchin embryos.

Figure S6 (Related to Figure 4, 5 and 6) : Influence of different parameters on the prediction of sea urchin cleavage patterns and early embryogenesis.

Figure S7 (Related to Figure 7): Influence of surface polarity conditions on ascidians cleavage pattern.

II. Supplementary Table

Table S1 (Related to all Figures): Parameters used to generate blastomere shapes throughout the manuscript from the Surface Evolver.

III. Supplementary Movie Legends

Movie S1 (Related to Figure 1). Typical sequence for the computation of blastomere shapes by "The surface Evolver". Example taken here correspond to the 4-cell stage zebrafish embryo.

Movie S2 (Related to Figure 2)3D rotation of model predictionsfor the cleavage pattern of fish embryos.

Movie S3(Related to Figure 2) 3D rotation of model predictionsfor the cleavage pattern of amphibiansembryos.

Movie S4(Related to Figure 2) 3D rotation of model predictionsfor the cleavage pattern of echinodermembryos.

Movie S5(Related to Figure 2) 3D rotation of model predictionsfor the cleavage pattern of ascidiansembryos.

IV. Description of the starter package (Supplementary Item S1, download separately, related to experimental methods)

V. Supplementary Methods

VI. Supplementary References

3-Supplemental Figures and Figure legends

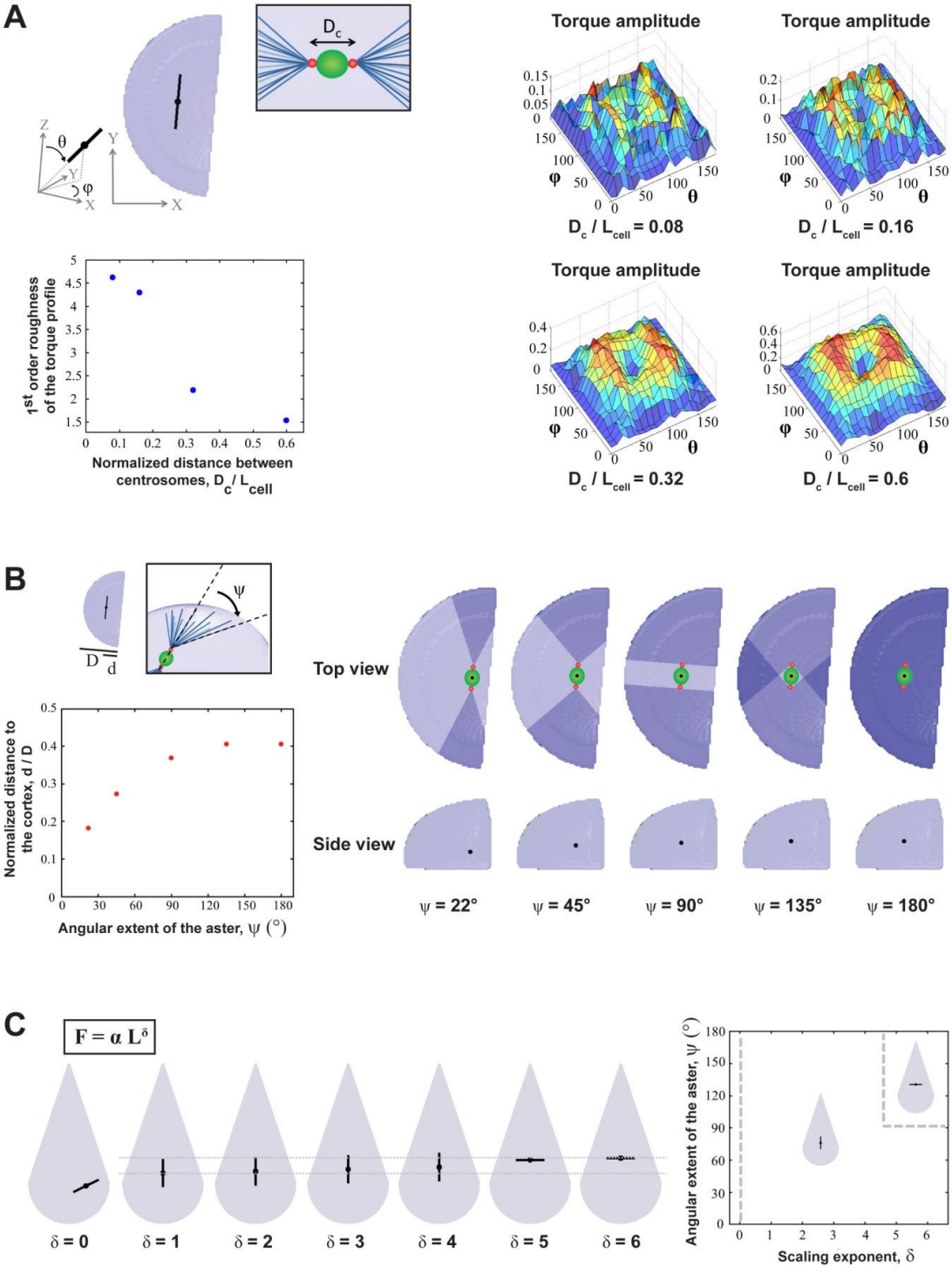

Figure S1 Pierre et al.

<u>Figure S1 (related to Figure 1)</u>: Influence of different parameters on the length-dependent model in 3D

(A) Influence of the distance between centrosomes D_c. Test cell: zebrafish 2nd division. (Top Left) Predicted position and orientation of the spindle for every value of D_c. (Right) Torque amplitude profiles for different values of D_c. The (θ, φ) orientations where the torque amplitude is close to zero correspond to the equilibrium of the aster pair. The value of the stable equilibrium position does not change but the noise increases when D_c becomes small. (Bottom left) Noise quantification: Roughness of the torque profile vs D_c. **(B)** Influence of the asters angular extent ψ. Test cell: zebrafish 2nd division. (Bottom Left) Predicted positions of the aster pair center for different values of ψ. The center of the cell's center of mass is better found for asters that probe the whole cell (larger values of ψ). (Right) Side and top views of the predicted positions of the aster pair center (black dot) for different values of ψ. Asters are depicted in darker blue. **(C)** Influence of length-dependent exponent δ, on division axis position and orientation (for ψ = 157.5°), and phase diagram of stable orientations, for different values of δ and ψ.

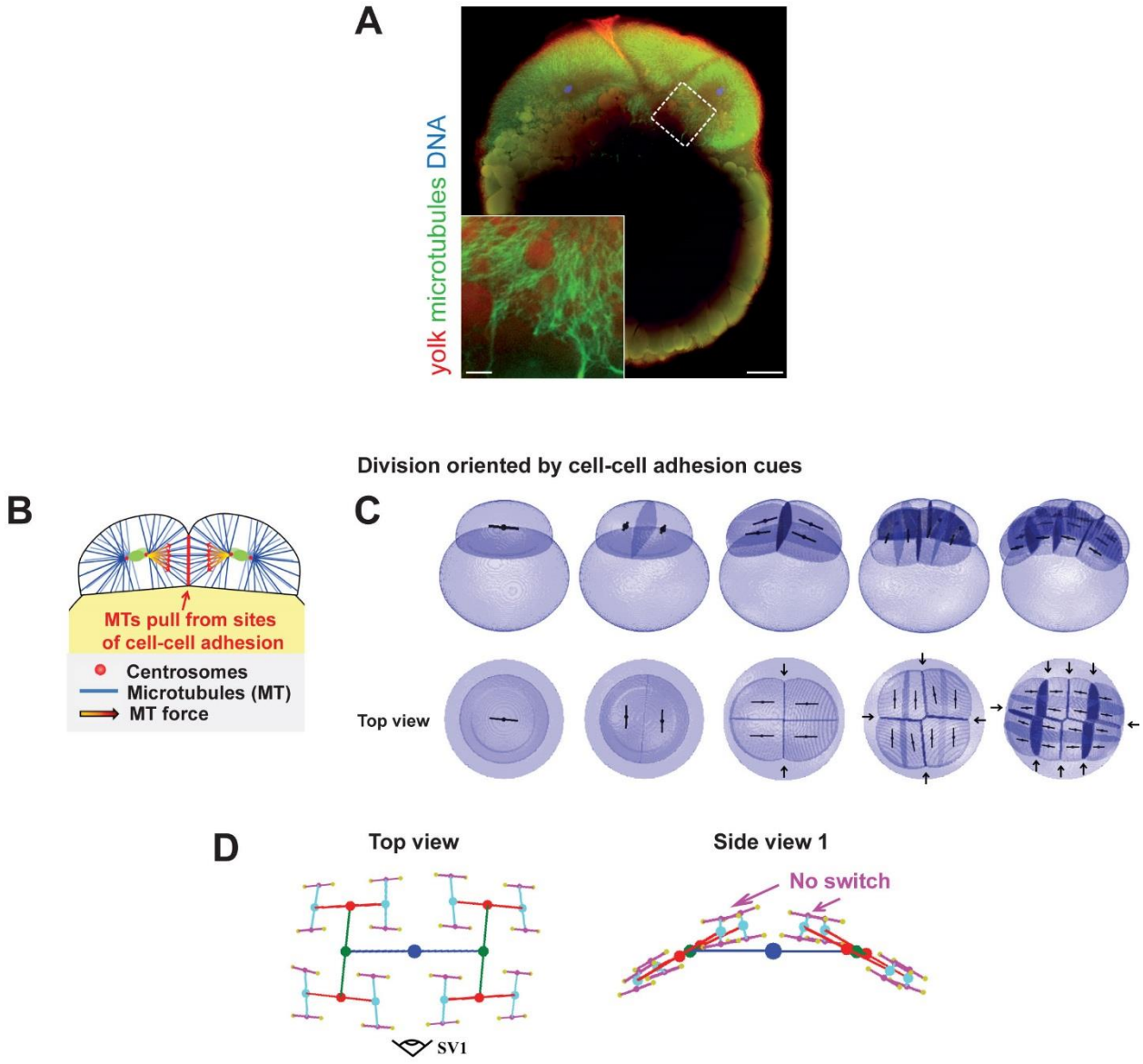

Figure S2 Pierre et al.

Figure S2 (related to Figure 2): Tests of hypotheses and parameters for zebrafish cleavage patterns.

(A) 4-cell stage zebrafish embryo expressing the MT marker ensconsin-GFP, fixed and labeled for actin and DNA, and imaged parallel to the A-V axis. Yolk granules fluoresce in the actin channel, and appear to exclude MTs. Scale bar: 50 μm, 10 μm (inset). **(B and C)** Predictions of the model, under the hypothesis that MT forces orienting the division axis arise from sites of cell-cell adhesion. Pulling interfaces (arrows) are depicted in darker blue. **(D)** The predicted cell division orientation lineage under this hypothesis. Note the absence of orientation switch at the 5^{th} Cleavage.

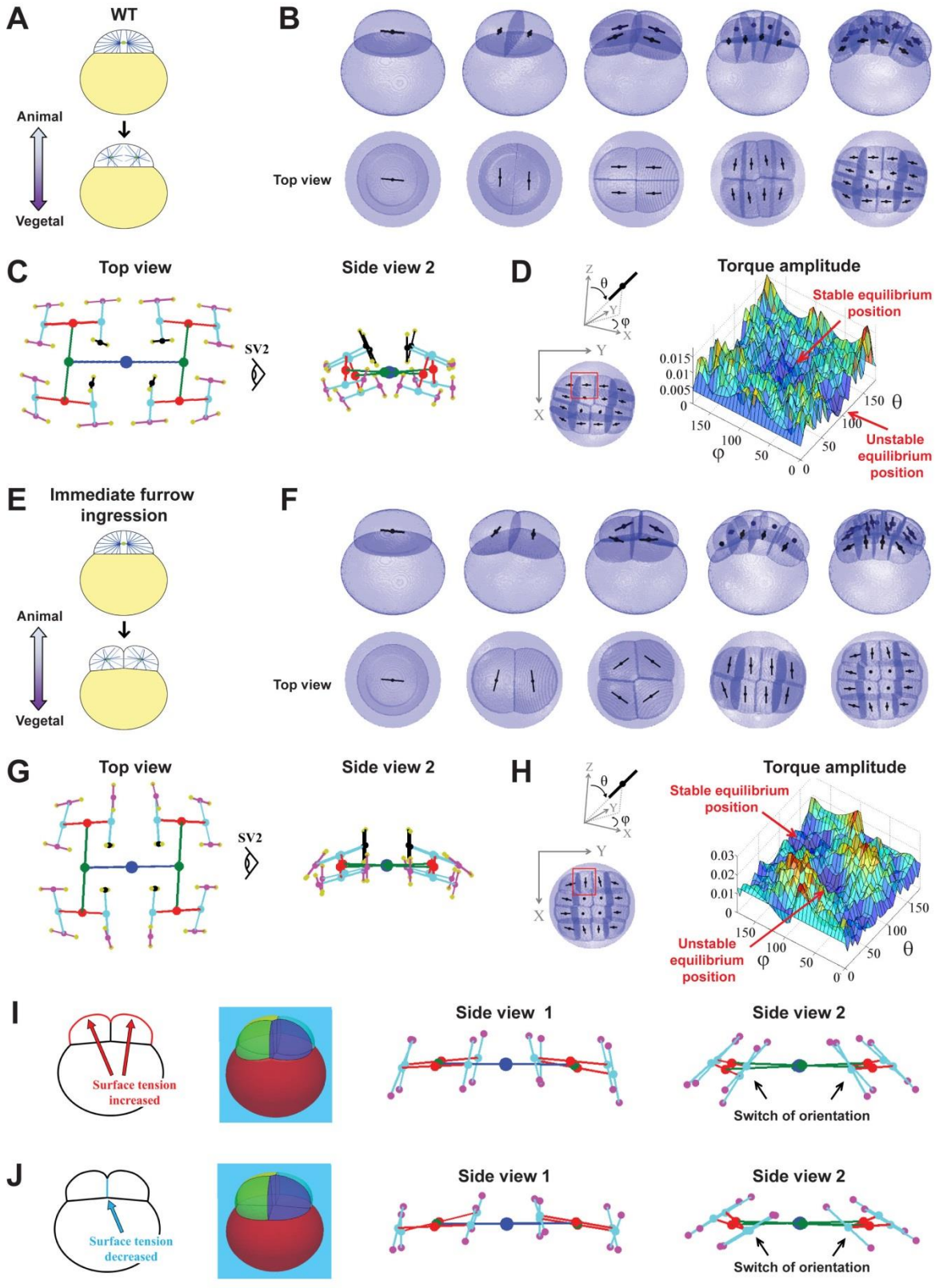

Figure S3 Pierre et al.

Figure S3 (related to Figure 2): Influence of shape parameters on the prediction of zebrafish cleavage and embryo morphogenesis.

(A-H) Test of the importance of delayed furrow ingression on cleavage patterns in fish. **(B-C)** Model predictions under a delayed cytokinesis hypothesis (also shown in figure 2). **(D)** Predicted orientation of the fifth division of a lateral external cell (highlighted in red) under this hypothesis, and corresponding torque amplitude profile, smoothed from half-size mesh (see Supplemental Information, p.3). **(E-H)** Test of a hypothesis of immediate furrow ingression preceding division axis setting in the next cell-cycle. **(F and G)** Predicted cleavage patterns. Note the different orientations at the 16 cell stages as compared to Figures S3B-S3C. **(H)** Predicted orientation of the 5^{th} division of a lateral external cell (highlighted in red) under this hypothesis, and corresponding torque amplitude profile, smoothed from half-size mesh. **(I)** The surface tension of the cell-medium interface γ_{ext}, is increased in the "Surface Evolver" model. This yields blastomeres that are too high already at the 4-cell stage and a consequent division orientation along the A-V axis. **(J)** The surface tension of the cell-cell interface γ_{int}, is decreased in the "Surface Evolver" model. This yields blastomeres that are too high already at the 4-cell stage and a consequent division orientation along the A-V axis.

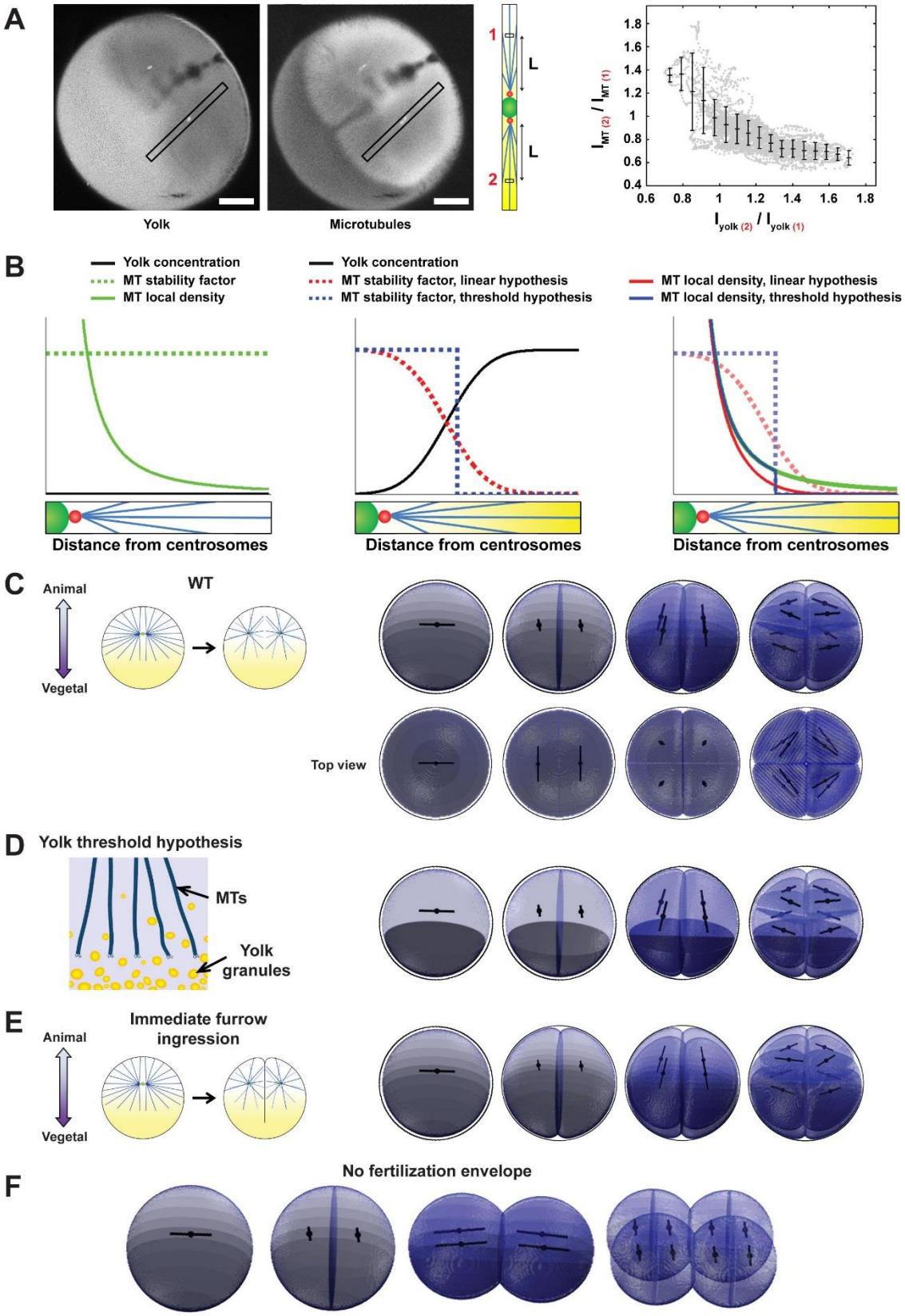

Figure S4 Pierre et al.

<u>Figure S4 (related to Figure 3)</u>: Influence of yolk and shape parameters on the prediction of Xenopus cleavage and embryo morphogenesis.

(A) Influence of yolk on MT density. (Left) Immunostaining images of a 2-cell stage Xenopus embryo, imaged near parallel to the A-V axis, depicting yolk (which fluoresces in the DNA channel) and MTs. Intensity profiles were extracted within the asters (boxes). Scale bar: 200 µm. (Right) Correlation between yolk and MT intensities, computed with regards to the distance to centrosomes, to avoid MT branching artefacts. $N_{profiles} = 45$, $N_{embryos} = 11$. Error bars are standard deviation. **(B)** Computed influence of yolk on MT density. (Left) Plot of the density of MTs as a function of the distance to the centrosomes, caused by pure dilution effects (no yolk). (Middle) Plot of yolk concentration as set in the model, and consequent evolution of the effect of yolk on MT density, based on a linear effect of yolk (red) or a threshold (blue). (Right) Combined effect of dilution and yolk on MT density, based on a linear effect of yolk (red) or a threshold (blue). **(C-D)** Test of different hypotheses for the impact of yolk on MT stability. **(C)** MT growth is inhibited in a dose-dependent manner by yolk concentration. (similar to Figure 3C) **(D)** MTs fully penetrate in the yolk up to a threshold in yolk concentration that stops MT growth. Note that the predicted cleavage pattern is similar to the one obtained in the previous hypothesis. **(E)** Test of a hypothesis of immediate furrow ingression preceding division axis re-orientation in the next cell-cycle on predicted cleavage patterns. Note that the pattern is similar to the one obtained in Figure 3C. **(F)** Predictions of the model with no confinement by the fertilization envelope in "The Surface Evolver". Note that blastomere shapes are completely different, and as a result, division axes do not switch orientation along the A-V axis at the 3rd cleavage.

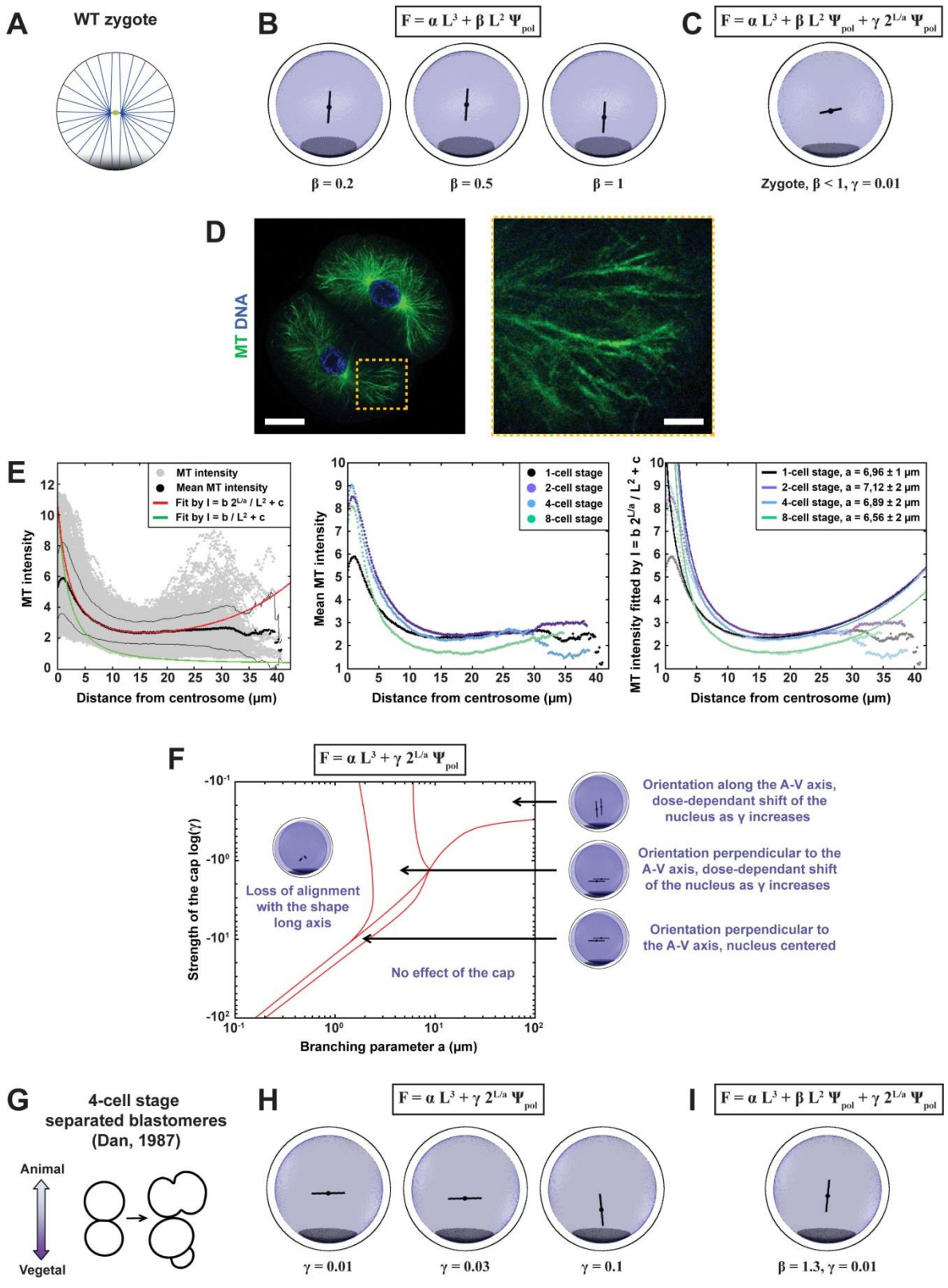

Figure S5 Pierre et al.

<u>Figure S5 (related to Figure 4, 5 and 6)</u>: Evidence and characteristics of MT branching in interphase asters in sea urchin embryos.

(A-C) Requirement of the exponential term (condition 2) for the influence of polar domain on MT force to obtain division axis oriented parallel to the domain. **(B)** Prediction of the 1st division relative to the polar domain, using only the dynein-limited hypothesis (condition 1). Note that increasing the parameter β causes division center to come closer to the domain, but does not create an orientation parallel to the domain. **(C)** Adding the exponential term (condition 2) allows to stabilize the parallel configuration. **(D)** Immunostaining image of a 2-cell stage sea urchin embryo in interphase, showing MTs (green) and DNA (blue). Scale bar: 20 µm (left), 5 µm (right). **(E)** MT intensity profiles show an exponential increase in MT density, which compensates dilution of MTs and is independent on cleavage stage. (Left) MT intensity profiles from the centrosome in 1-cell stage interphase embryos (gray), mean and standard deviation (black). $N_{profiles}$ = 368, $N_{embryos}$ = 10. Fit by L^2 cytoplasmic dilution with exponential increase (red). L^2 cytoplasmic dilution alone is shown in green. (Middle) Mean MT intensity profiles from the centrosome in 1 to 8-cell stage interphase embryos. $N_{profiles}$ = 368, 325, 117, 96, $N_{embryos}$ = 10, 10, 4, 10. (Right) Fits of MT intensity profiles in 1 to 8-cell stage by L^2 cytoplasmic dilution with exponential increase. The branching parameter, a, does not vary significantly between different stages. **(F)** Phase diagram of the predicted division positioning with only the exponential term in the model, for the 1^{st} and 2^{nd} divisions. **(G)** 4-cell stage blastomere separation experiment, suggests that rounded separated blastomere may orient their division axis along the A-V axis even without the influence of an elongated cell shape (Dan, 1987). (**H)** Prediction of the model for a separated 4-cell stage blastomere (round cell with size and β as in 4-cell stage), using condition 2 alone can only produce divisions parallel to the domain or asymmetric divisions. **(I)** The use of both conditions allows to produce symmetric divisions oriented towards the domain.

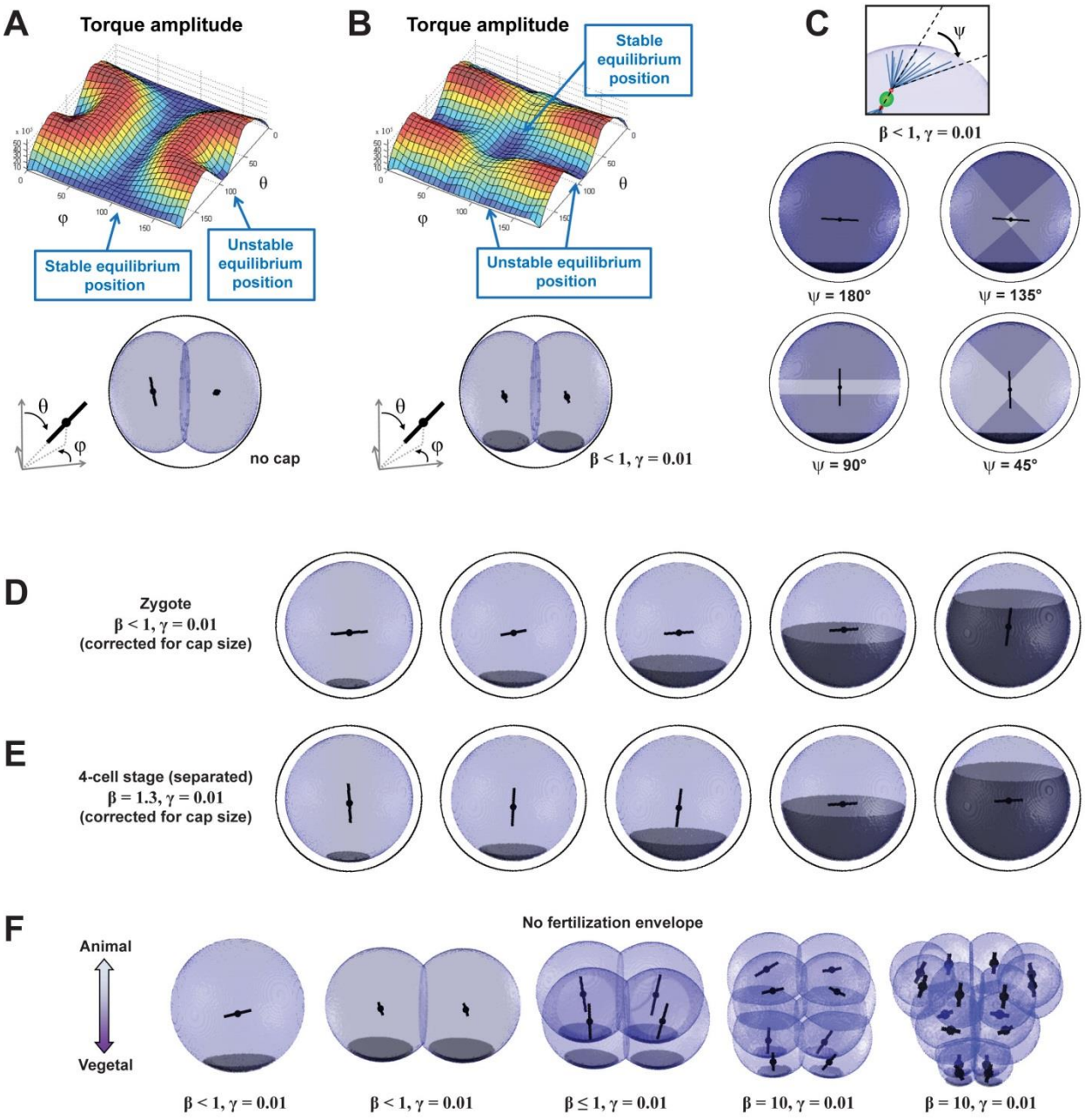

Figure S6 Pierre et al.

<u>Figure S6 (Related to Figure 4, 5 and 6)</u> : Influence of different parameters on the prediction of sea urchin cleavage patterns and early embryogenesis.

(A) Predicted torque landscape at the 2-cell stage with no contribution from the polarity domain. Not that several stable equilibrium orientations are available, and as a result the two division axis are not necessarily coplanar. **(B)** Predicted torque landscape at the 2-cell stage with a relatively small contribution from the polarity domain, which allows to modulate the potential landscape so that only one orientation parallel to the cap is now stable, yielding co-planar division axes. **(C)** Influence of the asters angular extent ψ, on the effect of polarity domain in the condition 1+2. The two asters must overlap to produce the 1st division orientation (parallel to the cap). Test cell: sea urchin zygote. **(D-E)** Influence of polarity domain size on division positioning, in the zygote **(D)** and in a separated round 4-cell stage blastomere **(E)**. Predicted orientation does not depend on cap size as long as the cap covers less than half of the solid angular surface seen by the aster center. **(F)** Model predictions are similar without confinement from the fertilization envelope. The same equation and parameters as in figure 5B are used.

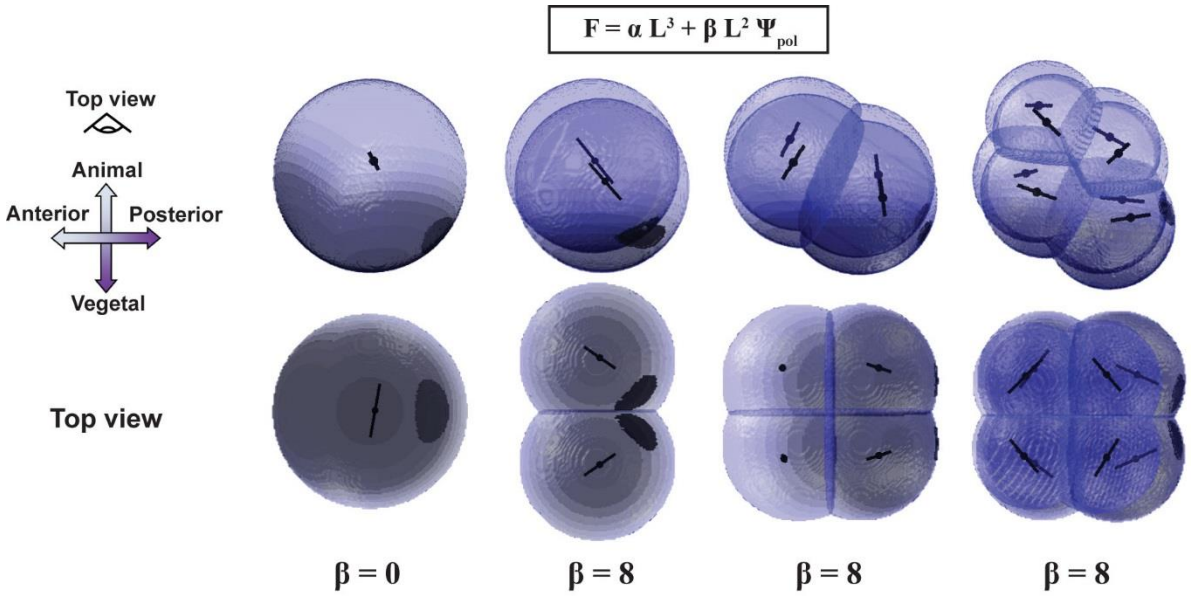

Figure S7 Pierre et al.

<u>Figure S7 (Related to Figure 7)</u>: Influence of surface polarity conditions on ascidians cleavage pattern.

The predictions of the model using only the condition (1) (dynein-limiting pulling) for domain influence on MT force is similar as when using both conditions (see Figure 7C).

2- Supplementary Tables and legends

	Confinement parameters	γ_{ext}	γ_{int}	γ_{int} new neighbors	γ_{cell_yolk}	$\gamma_{ext\ yolk}$
WT zebrafish (all cleavage stages) (Figures 2B and 2D)	R=0.684	2.4	1.5	1.9	3.3	3.5
Zebrafish, γ_{ext} decreased (Figure 2E)	R=0.684	1.4	1.5	1.9	3.3	3.5
Zebrafish, γ_{int} increased (Figure 2F)	R=0.684	2.4	3	3.8	3.3	3.5
Zebrafish, γ_{ext} increased (Figure S3I)	R=0.684	4.4	1.5	1.9	3.3	3.5
Zebrafish, γ_{int} decreased (Figure S3J)	R=0.684	2.4	0.375	0.475	3.3	3.5
WT Xenopus 1, 2 cells (Figure 3C)	R=0.624	0.65	-	1	-	-
WT Xenopus 4, 8 cells (Figure 3C)	R=0.624	0.65	1	1	-	-
Hertwig, horizontal compression (Figure 3F)	Z = ± 0.4 R=0.75 (r=1.7)	0.65	0.8	1	-	-
Hertwig, vertical compression (Figure 3G)	Y = ± 0.35 R=0.78 to 0.81 (r=1.85)	0.65	0.8	1	-	-
Xenopus without envelope (Figure S4F)	-	0.65	1	1	-	-
WT sea urchin 1, 2, 16 cells (Figure 5B)	R=0.684	0.75	1.1	1.1	-	-
WT sea urchin 4, 8 cells (Figure 5B)	R=0.684	0.75	1.1	1.3 – 0.9	-	-

Hörstadius experiment 1, 2 cells, final shapes (Figure 6B)	R=0.684	0.75	1.1	1.1	-	-
Hörstadius experiment 4 cells (Figure 6B)	R=0.684	0.75	1.1	1.3 – 0.9	-	-
Dan experiment 2-cell stage (Figure 6D)	Z = ± 0.37	0.75	-	1.1	-	-
Dan experiment 4-cell stage (Figure 6D)	Z = ± 0.29	0.75	1.1	1.3 – 0.9	-	-
Dan experiment 8-cell stage (Figure 6D)	Z = ± 0.23	0.75	1.1	1.3 – 0.9	-	-
Dan experiment 16-cell stage (Figure 6D)	Z = ± 0.18	0.75	1.1	1.1	-	-
Sea urchin without envelope, 1, 2, 16 cells (Figure S6F)	-	0.75	1.1	1.1	-	-
Sea urchin without envelope, 4, 8 cells (Figure S6F)	-	0.75	1.1	1.3 – 0.9	-	-
WT and no CAB ascidian, 1, 2 cells (Figures 7C, 7D and S7)	-	0.75	-	1	-	-
WT and no CAB ascidian, 4, 8, 16 cells (Figures 7C, 7D and S7)	-	0.9	1	1	-	-

Where the elliptic confinement is $R^2 = X^2 + Y^2 + (Z * r)^2$, and the total volume of the embryo is 1.

Table S1 (Related to all Figures): Parameters used to generate blastomere shapes throughout the manuscript from the Surface Evolver.

3- -Supplementary Movie legends

Movie S1 (Related to Figure 1). Typical sequence for the computation of blastomere shapes by "The surface Evolver". Example taken here correspond to the 4-cell stage zebrafish embryo.

Movie S2 (Related to Figure 2) 3D rotation of model predictions for the cleavage pattern of fish embryos.

Movie S3 (Related to Figure 2) 3D rotation of model predictions for the cleavage pattern of amphibians embryos.

Movie S4 (Related to Figure 2) 3D rotation of model predictions for the cleavage pattern of echinoderm embryos.

Movie S5 (Related to Figure 2) 3D rotation of model predictions for the cleavage pattern of ascidians embryos.

4- Description of the starter package (Supplementary Item S1)

A starter package which includes explanation text files, Matlab scripts, and examples to implement both division predictions and "Surface Evolver" is associated to this work (Supplementary Item S1). This package contains the Matlab programs that were used to predict the position of the cell division plane in 3D, as well as a typical input folder. It also contains indications and tools to generate the shape and polarity inputs to this program from a Surface Evolver output file.

5- Supplementary Methods

a- Parameters used in the division axis prediction model:

The model predicting division position and orientation consists of computing the net force and torque created by a pair of MT asters (Figure 1A and 1B). Forces and torques are calculated from summing the contribution of all MTs in the aster pairs, based on hypotheses on single astral MT forces detailed in the main text. The positions of the centrosomes are first computed from a given division axis orientation and centrosome-centrosome distance, Dc (Figure S1A). The intersection

between MTs and the cell surface, and the consequent length of MTs and polarity effect are calculated for every 1° x 1° solid angle within the angular extent of the asters, ψ, by assuming a constant angular MT density (Figure S1B).

Directed search loop:

The search for mechanical equilibrium is done using a directed search strategy, initiated from the center of mass of the cell shape matrix with a random orientation. At each iteration MT forces are summed up to compute a net force and torque on aster pairs, and one of the coordinates of the aster pair axis and position, x, y, z, θ or φ, randomly chosen, is changed according to the force / torque direction calculated at the previous iteration, with a step size of 1 pixel for x, y or z and 1° for θ and φ. As the total egg diameter is ~140 pixels, pixel size is ~ 4.3 µm for zebrafish, ~ 8.6 µm for Xenopus, ~ 0.7 µm for sea urchins, and ~ 1.2 µm for ascidians. After calculation of the new force and torque, the force and torque vectors are decomposed into the coordinate system associated with the cell (see p.4). The force / torque component corresponding to the changed coordinate x, y, z, θ or φ is compared to its value before the change. If it does not change sign, or if it changes sign but becomes smaller in absolute values, the new position / orientation is kept as a starting point for the next iteration. Conversely, if it changes sign but becomes larger in absolute values, then the simulation comes back to the previous position/orientation to change randomly another coordinate. To prevent the search loop to remain trapped in non-relevant local minima, we assumed a non-zero probability (typically 2%) to maintain the new position and orientation even if not favorable. The correct equilibrium is then identified when a certain number of iterations (~ 500) yields similar position and orientation. The equilibrium position is usually reached within 2000 iterations. A maximum total number of 10000 iterations is allocated to the program to reach the correct equilibrium. If the equilibrium is not found passed this number, the simulations are re-started from a different initial orientation. If needed, the simulations can also be initiated from a different starting position than the center of mass of the cell. Due to pixel noise, the intrinsic error in the division simulation is about 5 pixels in position and 5° in orientation. As the modeling framework is iterative, the overall error may be slightly amplified at every round of divisions.

In order to validate the directed search strategy and to avoid metastable equilibrium positions, the torque amplitude profile can be computed after the search for the equilibrium position. The net torque is calculated for every 3D orientation (θ and φ, with a mesh size of typically 10° x 10°), at

the equilibrium position. If needed, the mesh size can be reduced (between 3° x 3° and 5° x 5°) to allow smoothing of the torque profile and reduce noise. We note that the zeros of the torque can correspond to stable or unstable orientations (Figure S5A and S5B). The unstable orientations are excluded by looking at the direction of the torque vector.

To predict the cleavage orientation based on a hypothesis of cell-cell contact-oriented division in zebrafish (Figure S2B-S2D), we kept the equilibrium position given by our model based on length-dependent pulling; and assayed orientation. We then varied only θ and φ in the directed search, to search for the equilibrium in orientation, assuming the MT force to be now proportional to L^2 for MTs that reach a cell-cell interface, and 0 otherwise.

Calculation of the net force and torque:

For a spindle orientation (θ, φ), the MT force vector is calculated for every 1° x 1° solid angle (θ_{MT}, φ_{MT}), with θ_{MT} varying between 0 and the aster extension ψ (Figure 1A). The MT length and the polarity contribution ψ_{pol} (when relevant) are obtained by computing the intersection of this solid angle with the cell surface. The pulling force of one MT is then:

$$\vec{F} = (\alpha L^3 + \beta L^2 \psi_{pol} + \gamma 2^{L/a} \psi_{pol}) \vec{u}_{MT}$$

where $\vec{u}_{MT}$ is the unit vector along the MT axis. The force is applied in the point C which marks the centrosome. The torque at the point O, which marks the center of the nucleus, is then written as:

$$\vec{T} = \overrightarrow{OC} \wedge \vec{F} = F D_c/2 \ \vec{u}_{ZMT} \wedge \vec{u}_{MT}$$

where (X_{MT}, Y_{MT}, Z_{MT}) is the coordinate system associated with the aster (Figure 1A). In order to direct the search for the equilibrium position, the force vector is decomposed into the coordinate system associated with the cell (X, Y, Z). $\vec{F}$ is first decomposed into the coordinate system associated with the aster (X_{MT}, Y_{MT}, Z_{MT}):

$$\vec{F}_{XMT} = F \sin(\theta_{MT}) \cos(\varphi_{MT}) \vec{u}_{XMT}$$
$$\vec{F}_{YMT} = F \sin(\theta_{MT}) \sin(\varphi_{MT}) \vec{u}_{YMT}$$
$$\vec{F}_{ZMT} = F \cos(\theta_{MT}) \vec{u}_{ZMT}$$

Similarly, the torque vector in (X_{MT}, Y_{MT}, Z_{MT}) is written as:

$\vec{T}_\theta = F_{XMT}\, D_c/2\ \ \vec{u}_{ZMT} \wedge \vec{u}_{XMT} = F_{XMT}\, D_c/2\ \ \vec{u}_{YMT}$
$\vec{T}_\varphi = F_{YMT}\, D_c/2\ \ \vec{u}_{ZMT} \wedge \vec{u}_{YMT} = -\, F_{YMT}\, D_c/2\ \ \vec{u}_{XMT}$

$\vec{F}$ is then decomposed into (X, Y, Z):

$\vec{F}_X = (\, F_{XMT} \cos(\theta) \cos(\varphi) - F_{YMT} \sin(\varphi) + F_{ZMT} \sin(\theta) \cos(\varphi))\ \vec{u}_X$
$\vec{F}_Y = (\, F_{XMT} \cos(\theta) \sin(\varphi) + F_{YMT} \cos(\varphi) + F_{ZMT} \sin(\theta) \sin(\varphi))\ \vec{u}_Y$
$\vec{F}_Z = (-F_{XMT} \sin(\theta) + F_{ZMT} \cos(\theta))\ \vec{u}_Z$

As $(\vec{u}_{XMT\_aster1},\ \vec{u}_{YMT\_aster1}, \vec{u}_{ZMT\_aster1}) = -(\vec{u}_{XMT\_aster2},\ \vec{u}_{YMT\_aster2}, \vec{u}_{ZMT\_aster2})$ and (θ, φ) define the direction of $\overrightarrow{OC}_1$ with C_1 the centrosome of aster 1, the previous equations are written for a MTs in aster 2 as:

$\vec{F}_X = (-F_{XMT} \cos(\theta) \cos(\varphi) + F_{YMT} \sin(\varphi) - F_{ZMT} \sin(\theta) \cos(\varphi))\ \vec{u}_X$
$\vec{F}_Y = (-F_{XMT} \cos(\theta) \sin(\varphi) - F_{YMT} \cos(\varphi) - F_{ZMT} \sin(\theta) \sin(\varphi))\ \vec{u}_Y$
$\vec{F}_Z = (\, F_{XMT} \sin(\theta) - F_{ZMT} \cos(\theta))\ \vec{u}_Z$

The net force and torque is the sum of the contributions of all MTs, so that:

$\vec{T}_{\theta\_net} = \Sigma_{\theta MT,\, \varphi MT} \,|\, \cos(\theta_{MT}) - \cos(\theta_{MT} - 1°) \,|\, (\ \vec{T}_{\theta\_aster1} + \vec{T}_{\theta\_aster2}\ )$
$\vec{T}_{\varphi\_net} = \Sigma_{\theta MT,\, \varphi MT} \,|\, \cos(\theta_{MT}) - \cos(\theta_{MT} - 1°) \,|\, (\ \vec{T}_{\varphi\_aster1} + \vec{T}_{\varphi\_aster2}\ )$
$\vec{F}_{X\_net} = \Sigma_{\theta MT,\, \varphi MT} \,|\, \cos(\theta_{MT}) - \cos(\theta_{MT} - 1°) \,|\, (\ \vec{F}_{X\_aster1} + \vec{F}_{X\_aster2}\ )$
$\vec{F}_{Y\_net} = \Sigma_{\theta MT,\, \varphi MT} \,|\, \cos(\theta_{MT}) - \cos(\theta_{MT} - 1°) \,|\, (\ \vec{F}_{Y\_aster1} + \vec{F}_{Y\_aster2}\ )$
$\vec{F}_{Z\_net} = \Sigma_{\theta MT,\, \varphi MT} \,|\, \cos(\theta_{MT}) - \cos(\theta_{MT} - 1°) \,|\, (\ \vec{F}_{Z\_aster1} + \vec{F}_{Z\_aster2}\ )$

Where $|\cos(\theta_{MT}) - \cos(\theta_{MT} - 1°)|$ is a correction factor introduced to keep a constant MT angular density within the aster.

Comparing F_{X_net} (respectively F_{Y_net}, $F_{Z\_net\ \_net}$, T_{θ_net}, $\_T_{\varphi\_net}$) before and after a change in the coordinate x (respectively y, z, θ, φ) allows to direct the search for the equilibrium position.

Calculation of the torque amplitude profile:

The torque amplitude profile was calculated along the two degrees of freedom, by varying θ and φ from 0 to 180°:

$$T = \sqrt{\left(\overrightarrow{T_{\theta\_net}}\right)^2 + \left(\overrightarrow{T_{\varphi\_net}}\right)^2}$$

In order to reduce noise, the mesh size could be narrowed and $\vec{T}_{\theta\_net}$ and $\vec{T}_{\varphi\_net}$ averaged over two or three angular steps (typically steps of 5° or 3° respectively, in both θ and φ) before calculating T.

Parameters of the length-dependent force contribution:

In the length-dependent force model, the dominant parameter for division plane specification is the shape of the cell, which influences the shape of asters; that we input from "the Surface Evolver" simulation. The size of the embryo is about 140x140x140 pixels, and normalized to the egg size in the MT length calculation (so that sizes of all stages are consistent). We note that the embryo is not resized to its actual size in µm (all lengths in the force calculation remain between 0 and 1). As a consequence, and for consistency with the starter package (Supplementary Item S1), parameters α, β and γ are given without resizing correction in the main text. However, the branching parameter *a*, which represents a biological length-scale, is corrected in the text to provide a value in µm. In the case of a delayed furrow ingression (zebrafish and Xenopus), the shapes generated with the Surface Evolver are divided in two to account for aster-aster repulsion. Using a Matlab script, the aster-aster interface plane is inferred from the position of the spindle in the previous division prediction (bisecting it perpendicular), and the corresponding voxels from the Surface Evolver simulation are labeled, allowing to define and separate the two half-cells via an ImageJ treatment.

The distance between centrosomes D_c appears to have no significant influence on the position and the orientation of the division axis (Figure S1A). It was generally set to 20 pixels (for an egg diameter of L_{cell} ~140 pixels), and reduced for smaller blastomeres: in the zebrafish blastodisc (Figure 2, D_c = 16 to 10 for 2-cell stage to 16-cell stage), the 8-cell stage cells in Hertwig's experiments (Figure 3F and 3G, D_c = 16), and the sea urchin micromeres (Figure 5, D_c = 16 and D_c = 12 for 8-cell stage and 16-cell stage).

The aster extension ψ has little influence on division axis position and orientation in the length-dependent forces model (Figure S1B). However, an overlap of the two asters ($\psi > 90°$) is required to orient the division axis parallel to the polarity domain in echinoderms (Figure S6C). ψ was thus

set to 157.5° for all simulations, except for Xenopus where it was set to 112.5° to better account for aster-aster repulsion (Figure 3A). For simplicity, the angular density of MTs was assumed to be constant within the aster.

The absolute MT nucleation angular density is a silent parameter in the model. The MT force was calculated in every 1° x 1° solid angle, within the aster. Using smaller angular steps did not affect the results of simulations (data not shown).

In the length-dependent MT force expression, $F = \alpha L^{\delta}$, α is a silent parameter, fixed to 1. The parameter δ has little influence on division axis determination, if strictly positive and inferior to 5 (Figure S1C, and data not shown). It was set to 3 in all simulations following reported estimations in the literature. In this report, this cubic term was suggested to be a putative result of limiting amount of dynein in the cytoplasm as compared to MT density, which makes portion of asters sensitive to the volume they explore rather than their length or surface (Minc et al., 2011).

Parameters for yolk gradients and influence on MT lengths:

For the simulations which account for a dose-dependent influence of yolk on MT stability and length (amphibians and ascidians), the yolk spatial concentration was simulated using an "error function" along the gradient axis, x: $[\text{ yolk }] = (1 - \text{erf} (\mu (x - \varepsilon) / (2 L_{cell}))) / 2$; with L_{cell}, the diameter the egg (~140 pixels), μ the sharpness of the gradient and ε its offset from the center of the egg. A linear gradient was also tested, which did not impact the results (data not shown). An additional parameter η was used to compute the sensitivity of MTs to yolk, which impacts the local angular density of MTs: $d_{angle}(x) = 1 - [\text{ yolk }] / \eta(x)$. As default we used a linear assumption for the input of yolk on MT stability, so that $\eta(x) = 1$. To assess a threshold hypothesis, we directly changed the yolk input to a near-Heaviside function, which is equivalent to changing the MT density to a Heaviside function.

In the force and torque calculation, the local yolk-related MT concentration was used to modulate the effective mean length of MTs in each 1°x1° solid angle.

The parameters μ and ε for the yolk gradient were inferred from the literature: in Xenopus, ε parameter was set from the AVCR of centrifuged embryos, and μ was then inferred from the AVCR in controls (Neff et al., 1984; Yokota et al., 1992). In ascidians, μ and ε were estimated from

previous reports, and then adjusted to fit the asymmetry of the 2nd and 3rd cleavages (Conklin, 1931; Negishi et al., 2007). μ and ε were chosen from a 2-parameters phase diagram going from 0.2 to 500 for μ and from -10 to 50 pix for ε (data not shown). The parameter μ was set to 5 in Xenopus and 10 in ascidians (also for the additional 45° gradient at the 1st division). To test the influence of gravity on AVCR in Xenopus, μ was varied from 0.2 to 500 (Figure 3D). The parameter ε was set to 0 in Xenopus and 30 pixels in ascidians (25 for the additional 45° gradient at the 1st division). To test the influence of MT stability on AVCR in Xenopus, η was varied from 0.1 to 50 (Figure 3E). It was set to 1 in all other simulations. When testing the threshold hypothesis in Xenopus, μ was set to 5000 and ε to 20 pixels, to get a near-Heaviside yolk distribution (Figure S4D).

Alternative hypotheses tested to account for echinoderms cleavage patterns (data not shown):

In order to model the division orientations in sea urchin embryos, we tested several hypotheses that could potentially define an A-V polarity.

We first looked at the possible mechanisms for micromeres formation.- We showed that a volumic attractive domain, gradually accumulating close to the vegetal pole had the same effect as a surfacic one, yielding a switch of orientation at the 4-cell stage and an asymmetric division at the 8-cell stage when the strength of the domain was increased. This attractive domain being equivalent to a repulsive domain at the animal pole, we modeled it using a yolk-like gradient as in Xenopus. However, we could only reproduce the sea urchin development by increasing the amplitude of the gradient (which may correspond to an increase of the quantity of attracting effectors), and not by sharpening the gradient (recruitment of diffuse effectors). Despite those findings, we chose to model polarity with a surfacic domain as this is more in agreement with detergent treatment experiments (Dan, 1979; Tanaka, 1976).

- We then asked if micromeres formation could result from a pure sizing effect, associated with an increase in blastomere surface/volume ratio as the embryo cleaves, potentially rendering surface polarity effects stronger as blastomeres become smaller. Micromeres could be generated, but the shift of the nucleus towards the vegetal domain was progressive and did not occur as abruptly as in experiments at the 8-cell stage. The range of parameters allowing a rather abrupt shift of the

nucleus was extremely narrow, suggesting poor biological robustness. We thus chose to introduce a timing in the strength of the polarity, which is largely supported by retardation experiments and cut-egg experiments (Dan and Ikeda, 1971; Hörstadius, 1939).

Next, we tested several hypotheses which could potentially account for the orientations of the 1st two divisions parallel to the cap.

- Setting a power law ($F = \alpha L^3 + \beta L^2 \Psi_{pol} + \gamma L^n \Psi_{pol}$) instead of an exponential law for MT pulling could reproduce the division orientations parallel to the cap for $n \geq 4$. The switch of orientation and the asymmetric positioning of the nucleus were not sharp enough for $n \sim 4$, but tended to occur more abruptly as n increased. We found that a value of $n > 10$ would be close to experimental behavior. In light of those analyses, we chose to use an exponential law, which is supported by the evolution of MT density with the distance from the centrosome, likely associated with MT branching (Figure S5D and S5E).

- We next considered a hypothesis based on a slight deformation of the egg that would orient the 2 first axes along the A-V axis because of geometric effects. Experimentally we computed shape anisotropies of many eggs, and found that it was smaller than 3%, and that the division axis was not correlated with this slight shape deformation.

- As shown in Xenopus, yolk gradients may also modulate aster shape, and influence division positioning. Although echinoderm do not show any known accumulation of yolk or internal vesicles, we tested the combined effect of a volumic repellant using a yolk-like gradient as in Xenopus and a polarity domain. We note that a volumic repellant on one side of the embryo is equivalent to a volumic attractant on the other side. A slight repelling gradient at the animal pole or at the vegetal pole was sufficient to reproduce the 1st two divisions. A strong repellant in the vegetal half of the embryo, in competition with an attractive polarity domain from the 1-cell stage also allowed to orient the divisions parallel to the domain. Then fading of the gradient could reproduce the switch of orientation at the 4-cell stage and the asymmetric divisions at the 8-cell stage, for a constant domain strength. Thus those designs could in principle account for echinoderm cleavage. However, given the results of detergent treatment experiments which inhibit coplanarity of the two first axes, we chose not to favor these hypotheses (Figure 4C) (Dan, 1979; Tanaka, 1976).

- We next modeled the effect of a surfacic repellant ($F = \alpha L^3 - \beta L^2 \Psi_{pol}$), in addition to the vegetal attractive domain. A repellant at the animal pole oriented the 1st two divisions parallel to the domain, but did not allow a switch of orientation at the 4-cell stage. We could reproduce the full normal developmental pattern of sea urchin embryos only when the repellant was also at the vegetal pole, through a cleavage stage-dependent competition between the two superimposed domains. Biologically, this design would amount to assume that a fraction of MTs may push at the domain and another fraction may pull; and that the ratio between those fractions evolve with cleavage stage. We consider this hypothesis still plausible, but we favored a hypothesis based on two different modes of pulling, as described in the main text, given the evidence that MT pulling dominates in this system (Minc et al., 2011; Tanimoto et al., 2016).

- Finally, we asked if a wide attracting surfacic domain ($F = \alpha L^3 + \beta L^2 \Psi_{pol}$) could account for the orientation of the 1st two divisions (similarly to Figure S6E). We could reproduce the whole sea urchin development with a cleavage stage-dependent competition between this wide cap and a vegetal attracting domain: either using a constant wide vegetal cap and a strengthening vegetal domain, or with a constant vegetal domain and a fading wide animal cap. Given that all experiments performed to date support the existence of a single vegetal domain of polarity in echinoderms, we did not favor this hypothesis.

Based on these analyses, we modeled the sea urchin early development using a single surfacic vegetal domain with two competing pulling contributions, as described in the main text.

Parameters for polarity domains and their influence on MT forces:

Polarity domains, used in the simulation for echinoderms and ascidians, were generated in the script by setting a center location for the domain and using a Heaviside profile to represent the distribution of concentration of polarity effectors from this center. Step or Gaussian profiles were also assessed, which did not influence the results (data not shown). The characteristic width of the domain, Δpol, is taken to match images in the literature, and performed by our means (Figure 4B) (Negishi et al., 2007; Peng and Wikramanayake, 2013). It is about 70x70 pixels in sea urchins zygote, and 20x30 pixels in the 2-cell stage ascidian (for an egg diameter L_{cell} ~140 pixels). In later stages, the position and size of the domain are inferred from the previous division in the simulation. Δpol had in general only a minor influence on the predictions (Figure S6D and S6E).

Astral MTs that contact the domain can pull with an additional force that arises from a contribution of a "sliding mechanism" and/or an "end-on mechanism" (see main text). The adjustable parameter for the sliding mechanism, β, is allowed to vary with cleavage stage to account for stage-dependent effects of the domain on aster positioning in both systems (Figures 5, 6 and 7). In sea urchins, we tested the influence of β on cleavage planes positions and orientations, by varying β from 0 to 100, for each stage, either with the L^2 mechanism alone or with both pulling mechanisms (for a = 6.75 µm and $\gamma = 0.01$) (data not shown). For the 1st and 2nd divisions, we noted that any value between 0 and 1 gave similar results. The simulations are shown for $\beta = 0$. The switch of division orientation at the 4-cell stage either requires a clear shape long axis (like in normal development), or a β parameter around 1 (like in dissociated 4-cell blastomeres). Thus, we set β to 1.3 for 4-cell stage separated sea urchins blastomeres (Figure S5G and S5H) and to 1 or 1.3 for mid stages in Hörstadius experiment (Figure 6B). For micromeres formation, the amount of asymmetry depended on β in a dose-dependent manner. According to the amount of asymmetry observed in the literature, we set β to 10 for both normal development and Hörstadius experiments. We note that the observed asymmetric divisions may also be reproduced by setting a higher value for β, but with assuming an additional steric exclusion between the nucleus and the cell cortex (data not shown).

In ascidians, β was set to 0 for the zygote and 8 from the 2-cell stage. As for sea urchins, β was varied from 0 to 100, for each stage, either with the L^2 mechanism alone or with both pulling mechanisms (for a = 6.75 µm and $\gamma = 0.01$) (data not shown). We note that β should be bigger than 5 for the CAB to have an effect on division orientation from the 2-cell stage. However, in the 2nd and 3rd division, it must not be higher than 10, not to completely override shape and yolk contributions. In the 4th division, the asymmetry depends on β parameter in a dose-dependent manner, and the observed asymmetry is reproduced for $\beta = 12 \pm 5$. In the inactive CAB simulations, β was set to 0.

The influence of the end-on mechanism parameters γ and a, were also tested in a dose-dependent manner and were fixed and kept small in order to modulate the geometrical effects without overriding it (Figures S6A and S6B). In echinoderms, the parameter a was set to 6.75 µm based on experimental results (using a px/µm size computed from the real egg size), and γ to 0.01 according to the a-γ phase diagram (Figures S5E and S5F). For simulations including only the dynein-limited

mechanism (Figure S5B), γ was set to 0. We note that a should be smaller than 8.5 µm to favor a parallel orientation of the division towards the cap. For a = 6.75 µm, γ must be between 0.005 and 0.02, so that the polarity has an effect on orientation, yet with the nucleus remaining as close to the cell center as observed in imaged embryos (Figures S5E and S5F). When testing the effect of the end-on mechanism alone, γ was varied from 0.01 to 0.1 (Figure S5H).

In ascidians, we kept the same values for parameters γ and a, as the end-on mechanism did not appear to have a dominant effect in this system (Figure S7). For the inactive CAB simulations, γ was set to 0 (Figure 7D).

b- Parameters used in The Surface Evolver to generate blastomere shapes and arrangements:

Three generic parameters influence the shape of blastomeres and their arrangement: the surface tension of the cell-medium interface γ_{ext}, the surface tension of the cell-cell interface γ_{int}, and the envelope confinement geometry (Maitre et al., 2015). In addition, to better account for certain observed blastomere arrangements, we sometimes used different values for the tension of cell-cell interfaces between newly formed neighbors ($\gamma_{int\ new\ neighbors}$) and old adhering neighbors. The values of parameters used for different embryos, cleavage stages and experimental set-ups are given in Table S1.

Additional specific settings:

- In zebrafish, we could not easily reproduce a flat yolk / blastodisc interface as in reported images (Olivier et al., 2010). The simulated interface tended to round up more, probably because active yolk / cytoplasm separation, adhesion and asymmetric ring constrictions cannot be reproduced by a surface equilibrium model. Thus, to accurately account for embryo morphogenesis, we modelled the yolk / cytoplasm interface as a membrane and allocated specific surface tension values: γ_{cell_yolk} and $\gamma_{ext\ yolk}$ to it. To reproduce the observed flattening of this interface and of the yolky part of the embryo, we then assumed different densities in the yolk (0.25) and in the blastodisc (0), and added gravity as an external force in “The Surface Evolver”. This causes the “yolk cell" to fall and slightly

flatten against the spherical confinement. The density of yolk and radius of confinement were adjusted so that the yolk flattening matches the experimental data, and that the confinement do not affect the blastodisc. In addition, we observed that the overall blastodisc appeared to slightly increase in size over the initial cleavage divisions, plausibly because of material transport from the yolk to the blastodisc in initial stages (Kimmel et al., 1995). Thus, the yolk/blastodisc ratio was set to 4 for the 1-cell stage, 3.34 for the 2-cell stage and 3 for the subsequent stages.

- In sea urchins, we kept a relatively mild confinement of the envelope, as removing the envelope does not appear to influence division patterns and blastomere shapes in experiments (Summers, 1993). Accordingly, removing the envelope in the model did not affect cleavage patterns (figure S6F). We also added a minor hypothesis on the spatial value of $\gamma_{\text{int new neighbors}}$ to better account for asymmetric new cell-cell adhesions observed at the 4 and 8-cell stage, which seems important to define the orientation of the symmetric division of animal blastomeres at the 8-cell stage. In the model, this amounts to set a cell-cell tension that is higher towards the center of the egg as towards the outside. For simplicity we used a step function centered in the mid-line between the inner and outer sides of the egg with two values $\gamma_{\text{int new neighbors max}}$ and $\gamma_{\text{int new neighbors min}}$.

6- Supplementary References

Conklin, E.G. (1931). The development of centrifuged eggs of ascidians. The Journal of Experimental Zoölogy *60*, 1-120.

Dan, K. (1979). Studies on unequal cleavage in sea urchins I. Migration of the nuclei to the vegetal pole. Development, Growth and Differentiation *21*, 527-535.

Dan, K. (1987). Studies on unequal cleavage in sea urchins III. Micromere formation under compression. Development, Growth and Differentiation *29*, 503-515.

Kimmel, C.B., Ballard, W.W., Kimmel, S.R., Ullmann, B., and Schilling, T.F. (1995). Stages of embryonic development of the zebrafish. Dev Dyn *203*, 253-310.

Maitre, J.L., Niwayama, R., Turlier, H., Nedelec, F., and Hiiragi, T. (2015). Pulsatile cell-autonomous contractility drives compaction in the mouse embryo. Nat Cell Biol *17*, 849-855.

Minc, N., Burgess, D., and Chang, F. (2011). Influence of cell geometry on division-plane positioning. Cell *144*, 414-426.

Neff, A.W., Wakahara, M., Jurand, A., and Malacinski, G.M. (1984). Experimental analyses of cytoplasmic rearrangements which follow fertilization and accompany symmetrization of inverted Xenopus eggs. J Embryol Exp Morphol *80*, 197-224.

Negishi, T., Takada, T., Kawai, N., and Nishida, H. (2007). Localized PEM mRNA and protein are involved in cleavage-plane orientation and unequal cell divisions in ascidians. Curr Biol *17*, 1014-1025.

Olivier, N., Luengo-Oroz, M.A., Duloquin, L., Faure, E., Savy, T., Veilleux, I., Solinas, X., Debarre, D., Bourgine, P., Santos, A., *et al.* (2010). Cell lineage reconstruction of early zebrafish embryos using label-free nonlinear microscopy. Science *329*, 967-971.

Peng, C.J., and Wikramanayake, A.H. (2013). Differential regulation of disheveled in a novel vegetal cortical domain in sea urchin eggs and embryos: implications for the localized activation of canonical Wnt signaling. PLoS One *8*, e80693.

Summers, R.G., Morrill J. B., Leith, A., Marko, M., Piston, D. W., Stonebraker, A. T. (1993). A stereometric analysis of karyokinesis, cytokinesis and cell arrangements during and following fourth cleavage period in he sea urchin, lytechinus variegatus. Development, Growth and Differentiation *35*, 41-57.

Tanaka, Y. (1976). Effects of the surfactants on the cleavage and further development of the sea urchin embryos 1. The inhibition of micromere formation at the fourth cleavage. Development, Growth and Differentiation *18*, 113-122.

Tanimoto, H., Kimura, A., and Minc, N. (2016). Shape-motion relationships of centering microtubule asters. J Cell Biol *212*, 777-787.

Yokota, H., Neff, A.W., and Malacinski, G.M. (1992). Altering the position of the first horizontal cleavage furrow of the amphibian (Xenopus) egg reduces embryonic survival. Int J Dev Biol *36*, 527-535.